X-ray-initiated photodissociation of the glycine molecule

Li Fang,[1,*] Hui Xiong,[2] Edwin Kukk,[3] Vladmire S. Petrovic,[4] and Nora Berrah[2]
[1]*Center for High Energy Density Science, University of Texas, Austin, Texas 78712, USA*
[2]*Department of Physics, University of Connecticut, Storrs, Connecticut 06269, USA*
[3]*Department of Physics and Astronomy, University of Turku, FI-20014 Turku, Finland*
[4]*PULSE, SLAC National Laboratory, Menlo Park, California 94025, USA*

(Received 24 April 2018; published 9 November 2018)

We investigated the charge distribution and dissociation dynamics of glycine (NH_2CH_2COOH) molecules irradiated with 310-eV x rays from the Advanced Light Source synchrotron. With simultaneous measurements of the fragment ion yield, dissociation angle, and kinetic energy, we were able to reconstruct a three-dimensional image of the x-ray-initiated molecular dissociation. Using coincidence and correlated analysis and applying a systematic comparison of properties of ion species, we partially disentangled the fragmentation pathways and identified the most probable fragmentation channels that lead to the observed fragment ions. In addition, we showed anisotropic angular distributions of dissociation subsequent to core-level photoionization and Auger decay and found an association between the initial bond-breaking sites and the kinetic energies of the final fragment ions.

DOI: 10.1103/PhysRevA.98.053408

I. INTRODUCTION

Molecular fragmentation is one of the fundamental phenomena in photoreactions. The nuclear dynamics subsequent to the photoionization plays a key role in determining charge redistribution and transfer, and hence the final ionic products [1–3]. The understanding of the fragmentation of the molecular ions subsequent to the initial photoionization may provide the foundation for the ultimate photocontrol of charge dynamics. Photo-induced charge redistribution and molecular dissociation of diatomic or triatomic molecule has been investigated vigorously [4–7]. Difficulties in disentangling different fragmentation pathways soar as the number of atoms in the molecule increases. Ion-ion coincidence technique has been used as a common method to distinguish ions of the same species originating from different fragmentation channels [8–10]. The correlations between different observables have enabled tools for further deconvolving the dissociation processes.

In this work, we investigated the fragmentation of glycine (NH_2CH_2COOH) molecules subsequent to core-level ionization. With momentum-imaging time-of-flight (TOF) spectroscopy and position-sensitive measurements, we were able to directly determine the kinetic energy (KE), the emission angle (in laboratory frame), and dissociation angle (between the final momentum vectors of the departing fragments) and thus reconstruct a three-dimensional image of the fragmentation. By comparing the correlated measurements of multiple observables, such as the KEs and the emission and dissociation angles for various coincidence channels, we determined the dominant fragmentation pathways that led to the observed fragment ions. With the information of partially disentangled fragmentation pathways, we further studied the trends in the energetics of the ion fragments and found associations between particular bond cleavages and the fragment KEs. We also determined the momentum angular distributions that imply a transient change in the geometry of the fragment molecular ions.

II. EXPERIMENTAL SETUP

The experiment was carried out at beamline 8 of the Advanced Light Source (ALS) at Lawrence Berkeley National Laboratory [11]. The nominal photon energy was 308 eV. Based on photon energy calibration using NEXAFS data, the actual photon energy was found to be 310 eV. Throughout this work, we use the calibrated value for the photon energy. Ion signals were collected and recorded by a TOF spectrometer equipped with a delay-line detector (RoentDek GmbH) for both time and position measurements, allowing resolving the dissociation angle and the KE simultaneously [12,13]. Gas-phase glycine was delivered by a heated oven assembly at an oven temperature of 130 °C−150 °C. The base pressure of the chamber is $\sim 1 \times 10^{-8}$ Torr. The x-ray beam intersects with the molecular beam at 90°, forming a plane that is parallel to the detector plane. The polarization of the x-ray beam is along the TOF spectrometer axis. With simultaneous measurements of ion positions on the detector plane and TOF, a three-dimensional (3D) distribution of angle and velocity can be directly obtained: the velocity projection on the detector plane is obtained from the ion position measurement, and the velocity along the direction perpendicular to the detector plane is obtained from the TOF measurement. The dead time of the detector is ∼10 ns.

III. EXPERIMENTAL RESULTS

In the current work, the predominantly $C\ 1s$ photoionization and the subsequent Auger decay lead to dications of the

*lifang@austin.utexas.edu

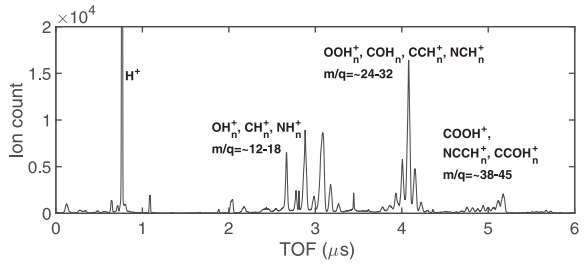

FIG. 1. Time of flight (TOF) spectrum of glycine irradiated with x ray at 310 eV.

polyatomic molecule which mostly dissociate in a concerted (simultaneous) or sequential manner. It is typical for an amino acid molecule, such as glycine, to lose neutral H pairs [14] and the dissociation can also release other neutral fragments that are not detectable in the current experiment. The photon energy used was above the 1s binding energy of C (292.3 eV) and below that of N (405.6 eV) or O (538.2 eV) atomic site in glycine molecule [15]. We confirmed that the first step of the dissociation is dominated by the bond breaking between the carboxyl (COOH) and the amino (NH_2CH_2) groups, as reported in previous work [14]. The resulting large fragment ions can undergo further, secondary dissociation. We have observed fragment ions of large (m/q [mass/charge] $\geqslant$ 38 amu), medium (32 amu $\geqslant$ m/q $\geqslant$ 24 amu), and small (m/q = 12−18 amu) sizes (see Fig. 1).

To show the different dissociation channels of the ion fragments, ion-ion coincidence analysis was applied and the results are shown in Fig. 2 as a photoion-photoion coincidence (PIPICO) map, where each panel shows coincidences between ions of different m/q ranges. The TOF of the ion species depends on their mass-to-charge ratio. In this work, we only investigate the ions with a charge of +1 and therefore will refer to all ions and their positions in the TOF spectra and in PIPICO maps by their mass only. All masses will be given in atomic mass units. As seen in Fig. 1, mostly midsize and small-fragment ions, e.g., CO^+, $NCH_n{}^+$, and atomic ions, were produced. Only a small amount of $NH_2CH_2C^+$ (around $m = 42$) was produced. Figure 3 shows the integral ion yield of the dominant coincidences, exhibiting that a large number of C^+ and O^+ ions were produced.

As seen in Fig. 2(a), in the first step of the fragmentation, the amino group is likely to lose two H atoms, resulting in the main contribution of $m = 28$; the carboxyl group is more stable at 45 amu. There is, however, also subsequent dissociation of the carboxyl group, which produces CO^+ or COH^+ and leads to a strong correlation between $m = 28$ and $m = 28$ or 29, as shown in Fig. 2(c). Continued dissociation of the carboxyl group also releases an O^+ ion or OH^+ ions, contributing to the strong correlation between $m = 28$ and $m = 16$ or 17, as shown in Fig. 2(d). Another fragmentation pathway that leads to coincidences between intermediate ions, such as those of $m = 16-18$ and $m = 28$, is bond breaking and charge separation that lead to doubly charged carboxyl groups. This channel with asymmetric charge distribution, i.e., the two charges are localized at one fragment, was determined to be the dominant pathway to producing intermediate fragment ions. In the coincidence map of the smallest ions,

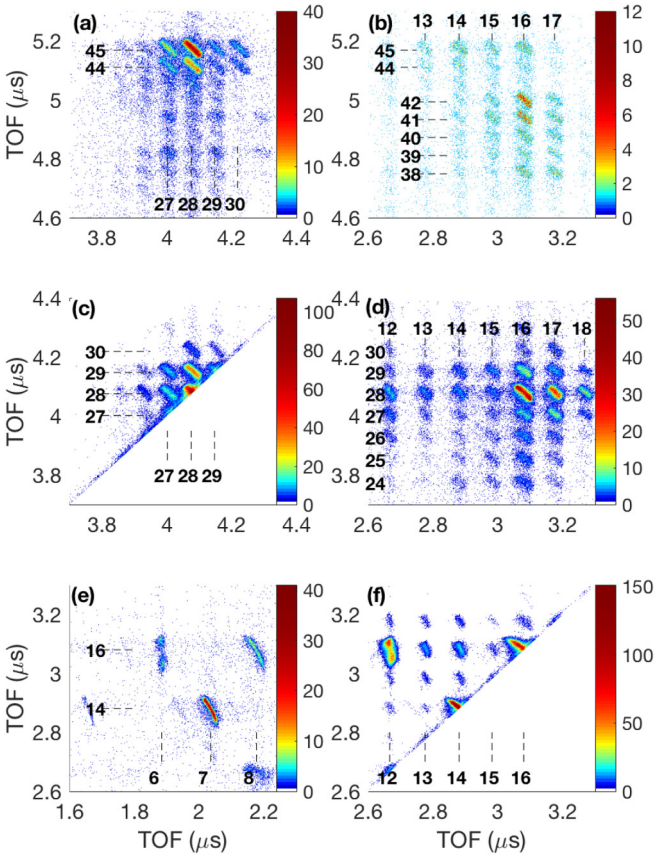

FIG. 2. Photoion-photoion coincidence (PIPICO) false-color map of glycine. Panels (a)–(f) show different regions of the time-of-flight range covered by the experiment. Dashed lines and labels indicate the corresponding m/q positions. The coincidence counts color scale is given at the right of all the panels. See details in the text.

shown in Fig. 2(e), the coincidence events between $m = 16$ (O^+) and $m = 6$ (C^{2+}) likely originate from the dissociation of glycine in the trication state due to shake-up or shake-off processes [16]. Double Auger decay can also lead to

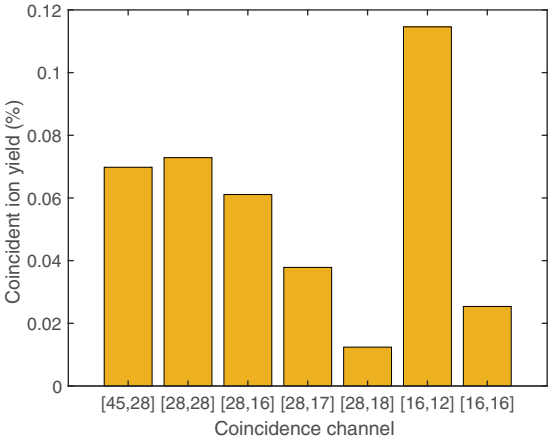

FIG. 3. Coincident ion pair yields normalized to the total coincident ion yield. Coincident events resulting from the ionization of the residual gas were subtracted.

TABLE I. Summary of fragmentation pathways for dominant coincidence channels. The angles are given relative to the vertical direction in the PIPICO map. The KEs are shown in parenthesis for an ion or shown after a plus sign for a total KE released in a bond cleavage channel. The KEs are given as peak KE, FWHM KE from the KE distribution as indicated, or KE from TOF projection (see text). The FWHM of the dissociation angular distribution is obtained from the data shown in Fig. 7.

Coincidence	Angle (°)	Slope (tan)	Mass ratio	Dissociation (Diss.) pathway and kinetic energy	Diss. angular FWHM
$m = [12, 16]$ $[C^+, O^+]$	10.5 ± 2.5	-0.18 ± 0.05	$C/NH_2CH_2COH = 2$	$NH_2CH_2COH^+ + O^+$(10-eV peak) $\rightarrow NH_2CH_2$+OH+C^+(2.5 eV FWHM)+O^+ $NH_2CH_2CO^+ + OH^+$(10-eV peak) $\rightarrow NH_2CH_2$+O+C^+(2.5 eV FWHM)+O^++H	97°
$m = [16, 16]$ $[O^+, O^+]$	57 ± 10	-1.5 ± 0.7	CO/O=1.75	$NCH_n + COO(H)^{2+}$ $\rightarrow NCH_n$+C+$O^+ + O^+$(up to ~30-eV peak)	
$m = [16, 28]$ $[O^+, CO^+]$	45 ± 3	-1.0 ± 0.1		$NCH_n + COO(H)^{2+}$ $\rightarrow NCH_n + O^+$(2-eV peak)+ CO^+(1-eV peak)	29°
$m = [17, 28]$ $[OH^+, CO^+]$	43 ± 4	-0.95 ± 0.15		$NCH_n + COO(H)^{2+}$+0.8 eV $\rightarrow NCH_n + OH^+(< 1\text{ eV}) + CO^+(< 1\text{ eV})$	49°
$m = [18, 28]$ $[H_2O^+, CO^+]$	45 ± 5	-1.0 ± 0.2		$NCH_n + COO(H)^{2+} + 0.7$ eV $\rightarrow NCH_n + H_2O^+(< 1\text{ eV}) + CO^+(< 1\text{ eV})$	46°
$m = [12, 28]$ $[C^+, CO^+]$	30 ± 3	-0.6 ± 0.1	CO/COO=0.6	$NH_2CH_2^+ + COO(H)^+$ $\rightarrow NH_2 + C^+(\sim 1\text{ eV}) + CO^+(\sim 1\text{ eV}) + O(H)$	51°
$m = [28, 28]$ $[NCH_2^+, CO^+]$	46 ± 5	-1.0 ± 0.2		$H_n + NCH_2CO^{2+} + O(H)$ $\rightarrow H_n + NCH_2^+(1\text{ eV}) + CO^+(1\text{ eV}) + O(H)$	46°
$m = [28, 45]$ $[NCH_2^+, COOH^+]$	43 ± 2	-1.0 ± 0.1		$H_n + NCH_2COOH^{2+}$+0.3 eV $\rightarrow H_n + NCH_2^+ + COOH^+ + 3$ eV	26°

trications and results in doubly charged fragment ions [17,18]. The coincidence events between $m = 14$ and $m = 7$ and the coincidence between $m = 16$ and $m = 8$ are contributions by the residual gas of O_2 and N_2. A particularly interesting peak is that of the coincidence between $m = 16$ and $m = 12$ (O^+ and C^+), as plotted in Fig. 2(f). As shown in Fig. 3, this coincidence accounts for a large contribution to the observed fragment ion abundance. We assigned $m = 16$ as O^+, because much less coincidence with $m = 13-15$ from CH_n^+ or NH_n^+ was observed. The "twisted bowtie" shape of this coincidence island indicates that the angle between the momenta of these two ions differed significantly from the antiparallel (180°). The abnormal shape is a result of sequential dissociations where the third fragments that carry away momenta are either not detected or not shown in a PIPICO map of two-body coincidence. As mentioned earlier, dissociating glycine molecular ions is likely to lose two H atoms, as indicated by the dominant peak at $m = 28$, either in self-coincidence or with the $COOH_2^+$ cation. However, in the dissociation that leads to $NCCH_n^+$ (m = ~40) and O^+ ($m = 16$), H atoms seem likely to remain attached.

In the coincidence map shown in Fig. 2, the slope of the pattern indicates the ratio of momenta of the faster and slower ions. A slope of -1 corresponds to equal momenta associated with a tail-to-tail two-body breakup, as shown by all the coincidences in Fig. 2(a). Widening of the island is due to the momentum gained by both ions in the coincident pair from the previous step in the sequential bond cleavages, typically due to releasing H atoms. Bond cleavages leading to large and intermediate fragments [Figs. 2(a)–2(d)] are dominantly associated with characteristics of two-body breakups. The pattern of coincidence between $m = 12$ and $m = 16$ [Fig. 2(f)] shows a large deviation from the -1 slope, indicating secondary dissociation after the initial charge separation. The angle of the slope for the coincidence island can be obtained by linear fitting or by rotating the island patch for the narrowest projection [14]. We applied both methods and present the values with smaller error bars. We selected the strongest coincidence islands in Fig. 2 and present the obtained angle of slopes for these coincidences in Table I.

We determined the KEs of all ions and their dissociation angles and emission angles based on the TOF and position measurements. The dissociation angle is defined as the angle between the momentum vectors of the two coincident fragment ions, and the emission angle is defined as the angle in the laboratory frame between the ion's momentum and the polarization direction of the radiation. Even with the same mass, ions from different dissociation channels may carry different KEs. Figure 4 exhibits the KE distribution for ions of two selected masses ($m = 28$ and 16) originating from various dissociation channels as labeled in the figure legend. For $m = 28$ (CO^+ or NCH_2^+), the KEs are similar and of about a few electronvolts for different channels. The channel that involves H_2O formation, i.e., releasing H_2O^+ ions, is associated with smaller KEs and a narrower KE distribution compared to the others [see Fig. 4(a)]. The KEs of O^+ ions possess a much stronger dependence on the dissociation channels, as seen in Fig. 4(b). Among the three selected channels, the KE of O^+ from coincidence [O^+, CO^+] has the smallest peak value and the narrowest distribution, while the KEs for the atomic

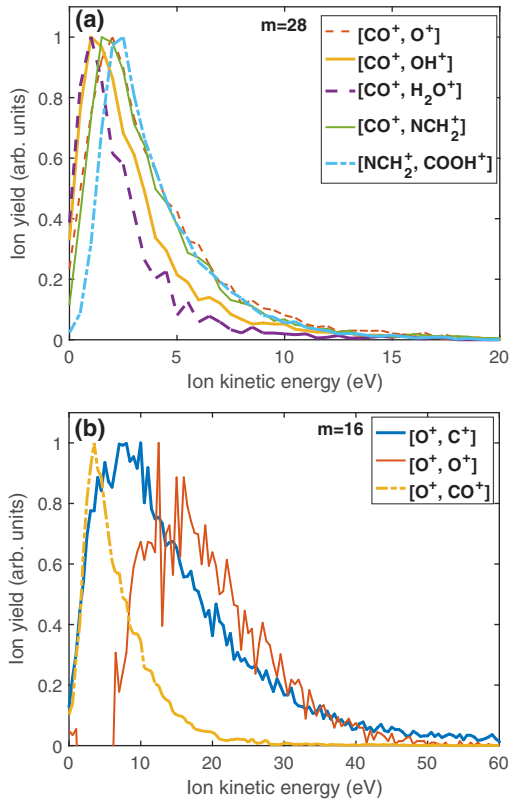

FIG. 4. Kinetic energy (KE) distributions of (a) $m = 28$ and (b) $m = 16$ from different ion-ion coincidence channels. Spectra are normalized to the peak height. In (b) the contribution from the residual background gas was subtracted for self-coincidence of $m = 16$; for all other coincidence channels, the contribution by the residual background gas was insignificant and can be neglected. The legends show the ion species of the dominant contribution to fragment ion yields.

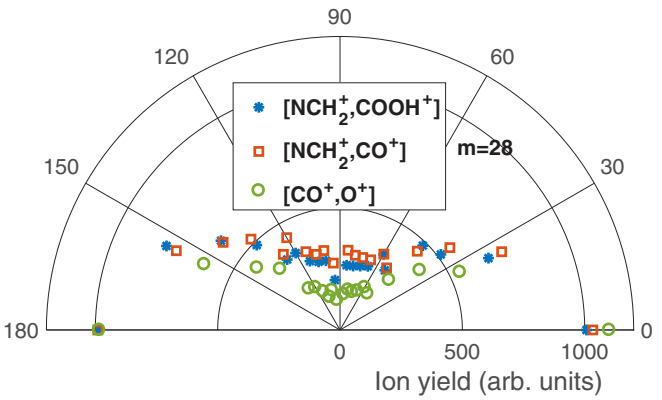

FIG. 5. Emission angle distribution of ion with $m = 28$ associated with different dissociation channels. The angle is relative to the polarization direction of the x rays. The distributions are normalized to peak values at 180°. The legends show the ion species of the dominant contribution to fragment ion yields.

coincidence channels $[O^+, O^+]$ and $[C^+, O^+]$ are significantly larger, associated with broad distributions. The dissociation channel of $[O^+, O^+]$ leads to a component of highly energetic O^+ ions and a very broad KE distribution.

Not only the KE but also the angular distribution provides information regarding the dissociation channels of the fragment ions. Figure 5 shows the emission angular distribution for ions of $m = 28$ originating from different dissociation channels. The emission angular distributions for channels $[NCH_2^+, COOH^+]$ and $[NCH_2^+, CO^+]$ are broader than that for channel $[O^+, CO^+]$, which has a characteristic of tail-to-tail dissociation of $COOH^+$. As expected, the emission angular distributions of the fragments of the same dissociation channel are similar due to conservation of momentum at the earlier dissociation stage, as seen in the angular distributions of NCH_2^+ and $COOH^+$ exhibited in Fig. 6(a). For coincidence fragments that went through multiple dissociation steps and were produced at the late stage of the dissociation, the emission angular distributions are likely to be different, as in the case shown in Fig. 6(b). The O^+ ions seem to be preferentially emitted along the x-ray polarization vector compared to the C^+ ions. As shown in Table I, O^+ is produced at an earlier dissociation stage than C^+ for this fragmentation channel.

The dissociation angle between two coincident ions exhibits a strong dependence on the dissociation channel and on the stage of the dissociation, as seen from Fig. 7. At the initial stage of the molecular dissociation where NCH_2^+ and $COOH^+$ were produced, the dissociation angle of the two ions is preferential around 180°, indicating a two-body breakup. At the intermediate stage where fragments, such as NCH_2^+ or CO^+, are released, the smaller angles start to contribute to the distribution. At the final stage, the atomic ions, such as C^+ and O^+, are produced, and the dissociation angular distribution extends significantly below 90°. The angular distribution of the dissociation of $COOH^{2+}$ into $[O^+, CO^+]$, through an intermediate stage, is the most closely confined at around 180°, just as its parent channel that produces the ion of $COOH^{2+}$.

We investigated further correlation between the emission angle and KE, as presented in Fig. 8, where the radius of the circle represents the KE of the ion and the azimuth is its emission angle. The number of ions observed at various KEs and emission angles is represented by a color scale. The upper and lower half-circles show the maps for the lighter and the heavier fragments, correspondingly. In these KE-angle correlation maps, a half-circular distribution indicates independence of KE on the emission angle. For all three coincidence channels shown in Fig. 8, the KE for ions emitted along the x-ray polarization direction is associated with a broader distribution than that of ions emitted at angles towards the perpendicular direction. The integral over all KEs as a function of the angle shows anisotropic distributions as mentioned above and shown in Figs. 5 and 6.

The deviation of the distribution of channels $[NCH_2^+, COOH^+]$, $[O^+, CO^+]$, and $[C^+, O^+]$ from a circular pattern, seen in Figs. 8(a)–8(c), shows that higher KE ions preferentially dissociate in the direction parallel to the x-ray polarization. The sequential dissociation that leads to O^+ is associated with stronger dependency of the KE on the emission angle compared to that of other fragments. The dissociation channel that leads to $[NCH_2^+, COOH^+]$ shows the least anisotropy than the secondary dissociation channels,

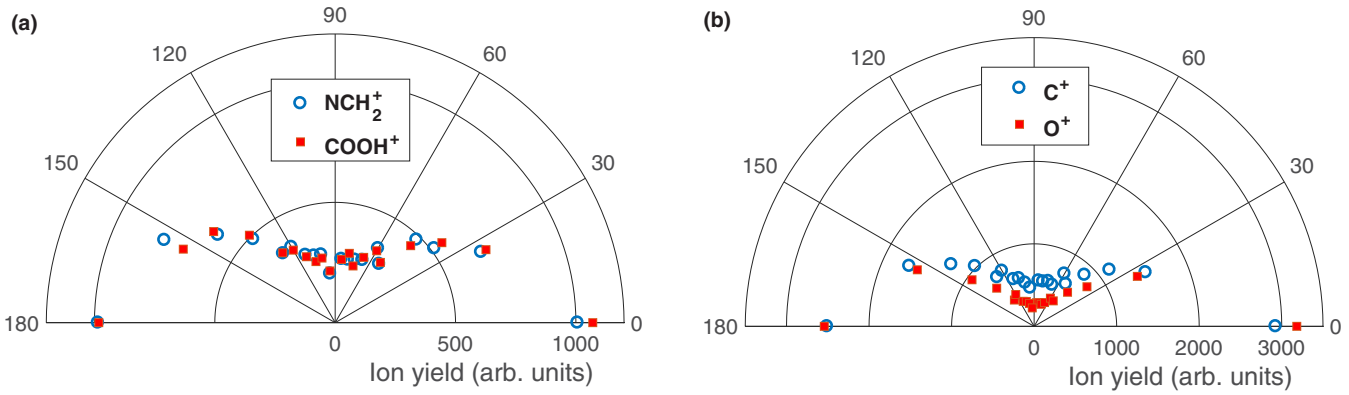

FIG. 6. Emission angle distribution of ion-ion coincidence between $m = 28$ and $m = 45$ and coincidence between $m = 12$ and $m = 16$. The distributions are normalized to peak values at 180°. The legends show the ion species of the dominant contribution to fragment ion yields.

as shown in Fig. 8. As seen in Figs. 8(b) and 8(c), while the emission angle dependence on the KE of CO^+ is comparable to that of O^+ in the coincidence of [O^+, CO^+], the correlation pattern of C^+ from the coincidence of [C^+, O^+] shows weak association between the angle and KE, dramatically different from the case for the other fragment O^+ where a strong dependence is seen.

As mentioned above, several observables, such as the ion abundance in a coincidence channel in comparison with that in adjacent coincidence channels, the KE, and the angular distribution provide information indicating their fragmentation pathways. Combining these measurements, we determined the most probable fragmentation pathways and summarize the KE and the widths of the angular distribution of the associated ions in Table I for the major channels. The ambiguity of the determination of species with a particular mass is minimized by considering the consistency in properties such as ion abundance and angular distribution of the ions differing by one or two H atoms only. For example, the mass of 16 in the coincidence between $m = 16$ and $m = 12$ can be assigned to O^+ or $NH_2{}^+$. Since the coincidence between $m = 12$, 14, or 15 is much weaker and does not have the twisted shape in the coincidence map (see Fig. 2), we presume that O^+ dominantly

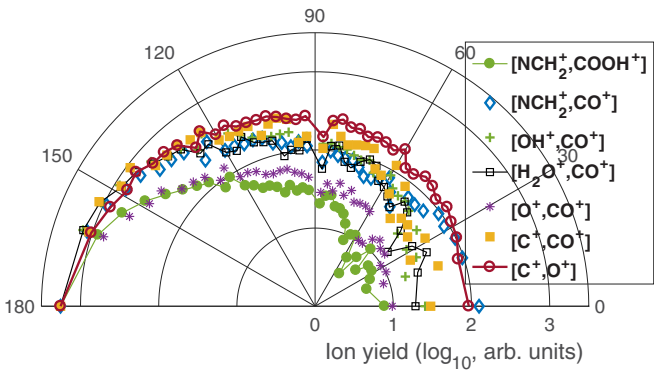

FIG. 7. Dissociation angle distribution of coincident fragment ions for different fragmentation channels, normalized to the highest values. The distributions are normalized to peak values at 180°. The ion yields are presented in log scale (see radial axis label) for clarity. The legend shows the main fragmentation channel to which the given fragments are assigned.

accounts for the ion signal of $m = 16$ in this coincidence. Similarly, for the coincidence between $m = 16$ and $m = 16$, O^+ is considered as the main contribution because the adjacent channels of coincidence between $m = 14$ and $m = 15$ or 16 are associated with low signal rates, different KE for $m = 16$, and different island slopes in the PIPICO map. The ion signal of $m = 28$ can represent a CO^+ contribution or a $NCH_2{}^+$ contribution. Based on the observation that the coincidence between $m = 26$ or 27 and $m = 16$ is almost absent (see Fig. 2), the dominant contribution to coincidence between $m = 28$ and $m = 16$ is likely to be [O^+, CO^+]. For this coincidence a few possible assignments of the dissociation pathways are as follows (the release of neutral H atoms is not included):

Sequential:

(1) $NCH_2COOH \rightarrow$(asymmetric charge distribution)
$NC(H_n) + COO(H)^{2+} \rightarrow NC(H_n) + O^+ + CO^+$

(2) $NCH_2COOH \rightarrow$(symmetric charge distribution)
$NCH_2{}^+ + COO(H)^+ \rightarrow NCH_2{}^+ + O^+ + CO$

Concerted:

(3) $NCH_2COOH \rightarrow NC(H_2) + O^+ + CO^+$

(4) $NCH_2COOH \rightarrow NCH_2{}^+ + O^+ + CO$

Since the dissociation angle of the two ions is associated with a narrow distribution along 180° indicating a tail-to-tail dissociation, (2)–(4) are less likely the responsible pathways than (1). The determination of concerted or sequential bond cleavage and the fragment assignment are also further supported by the estimated slopes for particular dissociations. For instance, for the pathway leading to [C^+, O^+], the first bond breaking results in equal momenta of the large fragment $NH_2CH_2COH^+$ and the lighter O^+, and the subsequent bond breaking of the large fragment will release a C^+ ion (and a neutral fragment) that carries part of the total momentum, proportional to the ratio of the mass of C to that of the total mass of the large fragment NH_2CH_2COH. This mass ratio was calculated and was found to match the measured slope tangent of the coincidence island, as shown in Table I. A similar argument can be made for coincidence between $m = 28$ and $m = 12$. The energy due to the release of a neutral element at an earlier stage of the dissociation was also estimated based on the width of the island along the shorter side in the coincidence map, as presented in Table I.

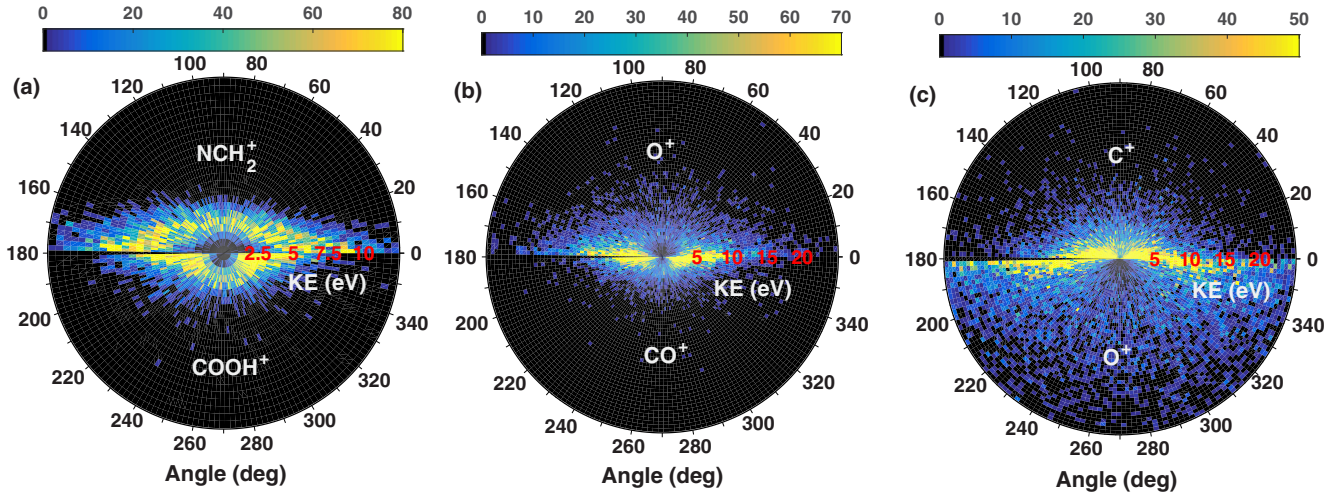

FIG. 8. Correlation between KE and the ion emission angle relative to the x-ray polarization. The upper and lower half-circles show the maps for the lighter and heavier fragments, correspondingly. The color represents the abundance of the ions (see color bars). (a) Coincidence between $m = 28$ and $m = 45$; (b) coincidence between $m = 16$ and $m = 28$; (c) coincidence between $m = 12$ and $m = 16$.

IV. DISCUSSION

Direct photoionization can lead to preferential ionization with radiation polarized along a particular molecular axis reflecting the shape of the ionized molecular orbitals [19,20]. Without molecular alignment, this angular preference relative to the molecular axis appears to be a preference relative to the photo beam polarization direction. Anisotropic ion angular distribution is not expected for core-level ionization due to the symmetric shape of the 1*s* orbital. Auger decay processes are also not expected to affect the ion emission angle in the laboratory frame, since these processes do not involve photons. Isotropic angular dependence in the laboratory frame was observed in small molecules, such as methane, following core-level ionization [21]. The dissociation angle between two fragments, on the other hand, reflects the original geometry of the molecule and is further affected by specific fragmentation pathways. The deviations in the dissociation angle from the geometry of the neutral molecules or parent ions are linked to the timescale of sequential processes during the dissociation and the transient geometry changes of the intermediate fragment ions [22].

The anisotropic emission angular distribution of coincident ions NCH_2^+ and $COOH^+$, shown in Fig. 6(a), is not expected for core-level ionization. For low-energy ions such as those from the coincidence of [NCH_2^+, $COOH^+$], the angular dependence of the detection efficiency is weak, since the TOF spectrometer is expected to have a 4π collection efficiency. Therefore the anisotropic angular distribution, as shown in Fig. 6, cannot be explained by instrumental artifacts. A tentative explanation is that the photon energy used is in the vicinity of resonant excitation. A previous work on C_2H_2 showed anisotropic ion angular distribution relative to the x-ray beam polarization due to resonant excitation of C at 311-eV photon energy [23]. However, our data taken at different photon energies also show anisotropic angular distributions.

The angular distribution of the subsequent dissociation in comparison with that of the previous step may reflect the natural geometry of the molecule or indicate changes in the geometry of the initial fragment ions. As shown in Fig. 6(a) and Table I, the first step of dissociation leading to NCH_2^+ and $COOH^+$ is associated with an emission angular distribution dominant along the polarization direction of the x-ray beam or a dissociation angle of 180°. Secondary dissociation of the NCH_2^+ and $COOH^+$ mainly contributes to the coincidence of [C^+, CO^+]. The [NCH_2^+, CO^+] coincidence originates from a similar initial dissociation but likely with an early release of OH (see Table I). The two coincidence channels share similar characteristics: a dissociation angular distribution peaking at around 180° and a similarly broader distribution. The preferred dissociation angle between CO^+ and C^+, mainly produced from the secondary dissociation of $NCH_2^+ + COOH^+$, reflects the initial geometry of the molecule and possibly a geometry change of $COOH^+$, and the broad distribution indicates that during the time of the secondary dissociation when each of the large fragment ions released a neutral constituent, the fragment ions had rotated away from their earlier orientation. The next bond breaking can also, though not dominantly, lead to C^+ and O^+, which could partially account for the dissociation angle around 90° for the coincidence [C^+, O^+] (see Fig. 7). In case of the first dissociation that leads to a neutral NCH_2 and a doubly charged carboxyl group $COOH^{2+}$, this channel is responsible for the coincidence of [OH^+, CO^+], [H_2O^+, CO^+], and [O^+, CO^+]. The dissociation angular distribution, almost identical for [OH^+, CO^+] and [H_2O^+, CO^+], shows a peak at 180° which is larger than the original geometry ~120° between the C–OH and C=O bonds [24]. The broad distribution could be an indication of the spread of a geometry change during the dissociation. In contrast, the coincidence of [O^+, CO^+] is associated with a narrow dissociation distribution at around 180°, differing by 60° from the neutral molecular geometry and resembling that for channel [NCH_2^+, $COOH^+$]. This may indicate that this channel is a fast dissociation channel associated with a quicker geometrical reorientation than the other two channels involving isomerization and water formation. As shown in Table I, the coincidence of [C^+, O^+] is determined

to be mainly from a unique dissociation pathway of molecular ions that lost an O^+ first. The dissociation angle between O^+ and C^+ peaks at around 180°, which is larger than the angle, about 120°–130°, between C–C and C–OH or C=O bond direction in the geometry of neutral glycine [24,25]. The much broader angular distribution implies that this dissociation channel is a slower process than other channels. Since C^+ and O^+ were produced at the last dissociation step, it is also possible that contributions from other pathways broadened the angular distribution as mentioned above.

Bond cleavage between the amino and carboxyl groups results in small ionic fragment KEs (see Table I). The large ion KEs are associated with a deferred charge separation: an initial asymmetric charge distribution that leads to a neutral amino group and doubly charged carboxyl group, in which case either the bond between the two groups or within the carboxyl group breaks first (see coincidence between $m = 16$ and $m = 12$) and coincidence between $m = 16$ and $m = 16$). The observation of highly energetic O^+ ions in the [O^+, O^+] channel [see Fig. 4(b)] is not easily explained. A point charge model of Coulomb repulsion between the two O^+ ions would render an initial separation of less than 1 Å. Hence, we consider the bond cleavage may occur in a short-range regime of the potential surface, resulting in the large dissociation energy.

V. CONCLUSION

We reported the investigation of charge distribution and molecular fragmentation pathways of glycine molecules irradiated with x rays at a photon energy above the 1-s ionization threshold of carbon. With the simultaneous measurements of the angle and KE and by the application of the ion-ion coincidence technique, we determined the dominant fragmentation pathways that led to the observed fragment ions. We found that the pathway leading to the dominant atomic ions starts with the cleavage of the double bond of oxygen atom within the carboxyl group. We also found the pathway resulting in water formation is associated with a bond-breaking between the amino group and the carboxyl group and an asymmetric charge distribution between the two large fragments. The determined dissociation pathways enabled us to investigate further how various events along the dissociation pathway affect the energetics of the fragment ions and their angular correlations. First major bond cleavage between the amino and carboxyl groups and dissociation involving water formation typically yields small KEs; whereas stripping off a doubly bound oxygen likely leads to highly energetic fragment oxygen ions. The changes in the dissociation angular distribution of the ions between the subsequent steps of bond cleavage indicates changes in the internal geometry of the fragment ions. This work also indicated unexpected anisotropy in the emission angular distributions of the fragmentations subsequent to core-level photoionization and Auger decay.

ACKNOWLEDGMENTS

We thank T. Osipov and C. Liekhus-Schmaltz for their assistance during the beam time. This work was funded by the Department of Energy, Office of Science, Basic Energy Sciences (BES), Division of Chemical Sciences, Geosciences, and Biosciences, under Grant No. DE-SC0012376. E.K. acknowledges support by the Academy of Finland. L.F. acknowledges support by the Defense Advanced Research Project Agency through Contract 12-63- PULSE-FP014, and by National Nuclear Security Administration through Cooperative Agreement No. DE-NA0002008.

[1] O. Travnikova, N. Sisourat, T. Marchenko, G. Goldsztejn, R. Guillemin, L. Journel, D. Céolin, I. Ismail, A. Lago, R. Püttner *et al.*, Phys. Rev. Lett. **118**, 213001 (2017).

[2] O. Travnikova, T. Marchenko, G. Goldsztejn, K. Jänkälä, N. Sisourat, S. Carniato, R. Guillemin, L. Journel, D. Céolin, R. Püttner *et al.*, Phys. Rev. Lett. **116**, 213001 (2016).

[3] E. Erk, R. Boll, S. Trippel, D. Anielski, L. Foucar, B. Rudek, S. W. Epp, R. Coffee, S. Carron, S. Schorb *et al.*, Science **345**, 288 (2014).

[4] A. Rudenko, L. Inhester, K. Hanasaki, X. Li, S. J. Robatjazi, B. Erk, R. Boll, K. Toyota, Y. Hao, O. Vendrell *et al.*, Nature (London) **546**, 129 (2017).

[5] P. Dietrich and P. B. Corkum, J. Chem. Phys. **97**, 3187 (1992).

[6] C. Jouvet, S. Martrenchard, D. Solgadi, C. Dedonder-Lardeux, M. Mons, G. Grgoire, I. Dimicoli, F. Piuzzi, J. P. Visticot, J. M. Mestdagh *et al.*, J. Phys. Chem. A **101**, 2555 (1997).

[7] L. Fang, T. Osipov, B. Murphy, F. Tarantelli, E. Kukk, J. P. Cryan, M. Glownia, P. H. Bucksbaum, R. N. Coffee, M. Chen *et al.*, Phys. Rev. Lett. **109**, 263001 (2012).

[8] J. H. D. Eland, F. Wort, and R. Royds, J. Electron. Spectrosc. Relat. Phenom. **41**, 297 (1936).

[9] C. E. Liekhus-Schmaltz, I. Tenney, T. Osipov, A. Sanchez-Gonzalez, N. Berrah, R. Boll, C. Bomme, C. Bostedt, J. D. Bozek, S. Carron *et al.*, Nat. Commun. **6**, 8199 (2014).

[10] T. Osipov, T. N. Rescigno, T. Weber, S. Miyabe, T. Jahnke, A. S. Alnaser, M. P. Hertlein, O. Jagutzki, L. P. H. Schmidt, M. Schöffler *et al.*, J. Phys. B **41**, 091001 (2008).

[11] https://als.lbl.gov/beamlines/8-0-1.

[12] Z. D. Pešić, M. Perri, R. Bilodeau, G. Ackerman, B. Rude, A. Kilcoyne, J. Bozek, and N. Berrah, J. Electron Spectrosc. Relat. Phenom. **155**, 155 (2007).

[13] D. Rolles, Z. D. Pešić, M. Perri, R. C. Bilodeau, G. D. Ackerman, B. S. Rude, A. L. D. Kilcoyne, J. D. Bozek, and N. Berrah, Nucl. Instrum. Methods Phys. Res. Sect. B **261**, 170 (2007).

[14] E. Itälä, K. Kooser, E. Rachlew, M. A. Huels, and E. Kukk, J. Chem. Phys. **140**, 234305 (2014).

[15] A. R. Slaughter and M. S. Banna, J. Phys. Chem **92**, 2165 (1988).

[16] T. Reich, P. A. Heimann, B. L. Petersen, E. Hudson, Z. Hussain, and D. A. Shirley, Phys. Rev. A **49**, 4570 (1994).

[17] J. H. D. Eland, P. Linusson, L. Hedin, E. Andersson, J. E. Rubensson, and R. Feifel, Chem. Phys. Lett. **485**, 21 (2010).

[18] P. Lablanquie, M. Khalal, L. Andric, J. Palaudoux, F. Penent, J.-M. Bizau, D. Cubaynes, K. Jänkälä, Y. Hikosaka, K. Ito,

K. Bučar, and M. Žitnik, J. Electron Spectrosc. Relat. Phenom. **220**, 125 (2017).
[19] P. Hoerner and H. B. Schlegel, J. Phys. Chem **121**, 1336 (2017).
[20] I. Thomann, R. Lock, V. Sharma, E. Gagnon, S. T. Pratt, H. C. Kapteyn, M. M. Murnane, and W. Li, J. Phys. Chem A **112**, 9382 (2008).
[21] E. Kukk, G. Prümper, R. Sankari, M. Hoshino, C. Makochekanwa, M. Kitajima, H. Tanaka, H. Yoshida, Y. Tamenori, and E. Rachlew, J. Phys. B **40**, 3677 (2007).
[22] R. Guillemin, P. Decleva, M. Stener, C. Bomme, T. Marin, L. Journel, T. Marchenko, R. K. Kushawaha, K. Jänkälä, N. Trcera *et al.*, Nat. Commun. **6**, 6166 (2015).
[23] J. Laksman, D. Céolin, M. Gisselbrecht, S. E. Canton, and S. L. Sorensen, J. Chem. Phys. **131**, 244305 (2010).
[24] G. M. Chaban, J. O. Jung, and R. B. Gerber, J. Phys. Chem. A **104**, 10035 (2000).
[25] M. Shmilovits-Ofir, Y. Miller, and R. B. Gerber, Phys. Chem. Chem. Phys. **13**, 8715 (2011).